

Multi vehicle adaptive 3D mapping for targeted ocean sampling

Tore Mo-Bjørkelund^{1,*}, Sanna Majaneva², Glaucia M. Fragoso², Geir Johnsen^{2,4}, and Martin Ludvigsen^{1,3}

¹Department of Marine Technology, Norwegian University of Science and Technology, Trondheim, Norway

²Department of Biology, Norwegian University of Science and Technology, Trondheim, Norway

³Arctic Technology Department, University Centre in Svalbard (UNIS), Longyearbyen, Norway

⁴Arctic Biology Department, University Centre in Svalbard (UNIS), Longyearbyen, Norway

*toremobjo@gmail.com

ABSTRACT

Expanding from profiling to three dimensional measurements of chlorophyll a using multiple underwater vehicles affords insights into a phytoplankton bloom. The context, variability, and uncertainty of a profile is often missed by traditional methods and an essential requirement for understanding ocean processes is the ability to measure their fine-scale variability. Phytoplankton distributions can be highly patchy and accurate identification of these patches and the environmental factors leading to their formation are hard to achieve. Traditional methods, such as plankton nets and *in-situ* vertical sensors, provide a snapshot and often miss the fine scale horizontal and temporal variability. Here, we show how two autonomous underwater vehicles measured and reported a real time data from a region in the upper water column in the high Arctic during a spring phytoplankton bloom. To gain the maximum available information, the vehicles moved in an adaptive fashion, seeking the regions of highest predicted chlorophyll a, greatest uncertainty, and least possibility of collision with other underwater vehicles and ships. Multiple autonomous underwater vehicles reporting spatio-temporal data in real-time for targeted water sampling can provide better match with sampling actions and plankton patchiness.

Introduction

Marine phytoplankton produce approximately half of the global oxygen¹ and measuring and mapping blooms of phytoplankton can be a challenge with traditional methods. Mapping of the dynamic conditions of a phytoplankton bloom has been attempted with autonomous underwater vehicles (AUVs)^{2–4} running adaptive sampling algorithms, where the robot adapts its path based on underway measurements. While previous efforts have been constrained to planar modelling of the environment, and assuming a static underlying field, we propose to expand the modelling to three dimensions and to take temporal effects into account. Expanding the number of robots affords a higher resolution of data collected, enabling accurate contextualization and foundation for decision making.

As the trophic base of nearly all marine ecosystems, phytoplankton act as a climate regulator by sequestering CO₂ to organic matter through photosynthesis, which can ultimately be exported to the deep ocean^{5,6}. Their community composition and timing of occurrences can be sensitive to climate change and environmental perturbation, impacting higher trophic levels, which can eventually cause an irreversible shift of the ecosystem^{7,8}. The spatial distributions of phytoplankton are highly heterogeneous⁹ and high density patches can occur at a vast range of spatial scales - from meso- to microscales¹⁰. Phytoplankton patchiness is driven by physical, chemical, and biological processes^{10–13}. The horizontal extent of these patches can be observed in surface waters by satellite images^{14,15}. Phytoplankton patchiness can exhibit as subsurface chlorophyll maxima, which is measured by vertical profiling sensors, limiting the three-dimensional understanding of patchiness below the surface. Traditional, ship-board net or water sampling for phytoplankton at pre-determined locations and depths provide integrated, or averaged, data that can miss high resolution structure of phytoplankton community, composition and abundance. In the Arctic, the common haptophyte *Phaeocystis pouchetii* can occur either as single cells or colonies up to three centimeter in diameter¹⁶, as well as forming high density blooms⁷. These colonies and blooms are often not fully resolved in space and time due to lack of sufficient resolution in the sampling.

Adaptive robotic sampling, using chlorophyll a estimated from fluorescence (CF) as a proxy for phytoplankton concentrations in ‘hot-spots’² has been suggested as solution for providing insights into their patchiness. CF measured in live phytoplankton cells using *in-situ* sensors can be used as a proxy of biomass, but values need to be verified from *in-vitro*

analyses of chlorophyll a from water samples. Therefore, combination of adaptive robotic sampling and physical sampling of phytoplankton is needed^{3,17}. However, by not sharing the data collected by the AUVs in real time, the ocean sampling is still done deterministically. Adaptive sampling, using AUVs for targeted measurements of the ocean^{2,4,18–26}, is a commonly used method for capturing dynamic and transient phenomena. In adaptive methods, path planning is often done by *deliberation* by a utility function evaluated along potential paths. The utility function needs a prediction of the distribution of the environmental variables of interest, such as salinity, temperature, and CF. Common modelling approaches are Gaussian processes (GP)²⁷ and higher order simulation models²⁸. Chlorophyll a estimation using a *log*-GP (ℓ GP) for estimation of the CF field and multi vehicle communication using asynchronous surfacing has been explored⁴.

The exploration problem with multiple sampling platforms was formalized in a sequential decision-theoretic planning under uncertainty framework termed the multi-robot adaptive sampling problem². For efficient multi vehicle adaptive sampling, data sharing between agents is essential for on-board model error reduction²⁹. Communication constrained multi vehicle sampling was investigated, and showed that error reduction of the on-board model is dependent on the quality of the communication between agents²⁹. Communication-constrained multi-vehicle operations were undertaken off the California coast, using a fleet of AUVs, communicating over the horizon by IRIDIUM®^{30,31}, the Autonomous Ocean Sampling Network-II deployed a multi-month mission to map coastal waters³², in an effort to develop a sustainable, portable, and adaptive ocean sampling system. The Adaptive Sampling And Prediction (ASAP) project³³ set out to monitor and coordinate a set of gliders using over the horizon communication.

As the spatio-temporal patchiness has a fundamental role in the functioning of marine ecosystems¹⁰, understanding the nature of their patchiness is needed to disentangle predator-prey interactions, and the flow of carbon through the food web. Here, we show how two AUVs reporting real-time data for targeted discrete water sampling can provide better match with sampling actions and fine-scale plankton patchiness. Further, by having the AUVs adapt their path and share measurements, they are able to effectively map the three dimensional extent and temporal variability of the patchy phytoplankton bloom. By combining adaptive robotic sampling with over the horizon satellite communication and a manned vessel, we created a heterogeneous sampling network for targeted sampling during a spring phytoplankton bloom (May 2022) in Kongsfjorden, Svalbard (Figure 2 a and b). Adaptive sampling is achieved by modelling the CF on board the AUVs using a ℓ GP², in three dimensions, with the AUVs seeking regions of high CF and high uncertainty, following the sense-plan-act cycle³⁴. Data is exchanged through the network over IRIDIUM®^{30,31} satellite link and displayed to the operators in a central operator hub. The human-crewed vessel acted upon the information gained by the autonomous agents for taking targeted and contextualized water samples. This three-dimensional reconstruction of phytoplankton CF patchiness evolving in space and time offer a unique opportunity to understand the mechanism underlying their heterogeneous distributions.

Results

Our approach is evaluated in three parts, (1) by simulating up to four AUVs in a common CF field, (2) by a field experiment, deploying the heterogeneous network and comparing the predictions from the AUV data to measurements and samples taken from a crewed vessel, and (3) by challenging the underlying assumptions of the distribution and statistical properties of the CF field. Hence, the results of convergence time in simulation, model performance compared to field measurements, and the statistics of the CF field are presented. This enables a critical look at the assumptions of the implemented ℓ GP.

Simulation

For development and testing of the algorithm for multi vehicle adaptive mission planning, simulation trials were used, simulating a bloom, based on expected values and distributions. The system enabled each vehicle in the heterogeneous network to make decisions *in-situ*, mapping the phytoplankton plume find a path that minimized uncertainty for the operation volume while seeking CF maxima. A single vehicle simulation over a $3000\text{m} \times 3000\text{m} \times 50\text{m}$ volume resulted in the on-board model predictive mean converging after 6000 – 7000 seconds, with the root mean squared error (RMSE) between the on-board model and the simulated field as the convergence criterion. When the single vehicle approach was compared with multi vehicle one, a significant gain in model accuracy and convergence time was observed when adding one vehicle. Further, the benefit of adding more vehicles diminished as the number of vehicles in the network increased. (RMSE results for one to four vehicles, Figure 1a). Using four vehicles, the RMSE converged to the nugget standard deviation of the models used in simulation, $\sigma_n = 0.7$.

Field deployment

The goal of the field trials was to estimate the three dimensional distribution of CF in the operational volume by using two AUVs, and to verify the adaptive on-board mapping algorithms and sensing network. Using the CF data from the AUVs, the ℓ GP was evaluated at each grid cell in the operational volume (Figure 2d and e). A horizontal slice taken in the interval $y \in [1200, 1500]\text{m}$ (Figure 2c and f) was taken to evaluate the area along the Northwestern edge of the operational volume near the point marked KB3. In both cases (Figure 2c-f), a clear vertical structure in the predicted CF was visible, with a low

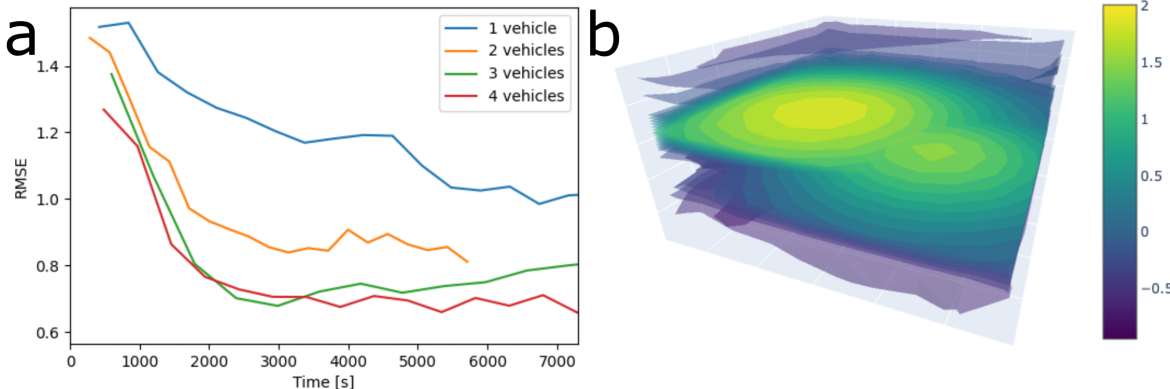


Figure 1. Simulation results and simulated CF field, (a) RMSE of on board models compared to simulated ground truth, of one to four vehicle missions of the same operational area and underlying simulated field. Simulated (b) chlorophyll-a fluorescence field, plotted on a $3000\text{m} \times 3000\text{m} \times 50\text{m}$ operational volume used for simulation. Plotted using log-scale for easier visualization.

concentration in the upper 15 – 20m, followed by a layer of higher concentration below 20m. In the horizontal plane, patchiness was also visible with a heterogeneous distribution without a clear trend. There is a sporadic discrepancy between the CF measurements and the underlying field, (for example at Figure 2c at 45m depth and $x \simeq 900\text{m}$), indicating noisy measurements and/or patchy distributions of CF.

To assess the on-board model, it is re-run in post processing, using input from both AUVs. The averaged model uncertainty for the on-board model decreases for the first 3000 seconds, before leveling off at around $2.5\mu\text{g}^2/\text{L}^2$ (Figure 3a). In addition to higher precision, the accuracy also increases with time (Figure 3b), with fewer and lower peaks of RMSE between instances of the ℓGP . The predicted CF profiles at station KB3 are plotted after each data exchange event (Figure 3c) as seen from the operator hub. The synthetic profiles follow the same pattern of low CF values in the upper 20m, with a wide maxima between 30 and 50m, showing little variation in the prediction as new data is gathered.

The ℓGP was evaluated at the sampling location (KB3^{35,36}), producing a predicted CF profile. To validate this profile, it was compared to the *in-situ* CF measurements from the fluorometer attached to the shipborne CTD and the *in-vitro* chlorophyll a values (4). These three independent profiles (CF prediction, CF measurement and *in-vitro* measurement) all showed the same trend in the water column. A CTD cast down to 300m showed low CF values near the surface down to 20m, and a subsurface maxima between 28 and 50m. Additionally, the shipborne measurements were noisy, likely caused by the combination of a small sampling volume for the fluorometer and the bloom being dominated by the colony forming *Phaeocystis pouchetii* (Figure 4b). Targeted water samples were taken at locations with both high and low CF predictions based on data from the AUVs (lowest 0 and 17m and highest 25, 37, and 50m). Values from the *in-vitro* chlorophyll a were approximate to the prediction from the ℓGP (Figures 3c and 4a). In the log-space (Figure 4a), the largest offset between the three profiles is in the upper 15m, where the values are the lowest. The prediction of CF, shipborne CF measurements and *in-vitro* chlorophyll a measurements follow each other closer in the deeper layers, below 15m. The uncertainty bounds on the predicted CF profile were wide in relation to the noise level on the ship borne CF measurements. This is coming from the temporal and spatial offset between the AUV measurements and the shipborne measurements in addition to the nugget effect noise. This indicates that the ℓGP was well configured and able to predict the *in-situ* and *in-vitro* values and uncertainties.

Statistical properties

Due to the "hot-spot" characteristics^{2,4,29} CF measurements in bloom conditions, we assumed that they would have a log-normal distribution. This assumption was confirmed by a best-fit analysis³⁷, evaluating log-normal, gamma, beta, Burr³⁸, and normal distributions (Table 1 and Figure 5a), using the sum of squared errors and the Akaike information criterion^{37,39}. From these analyses, the log-normal distribution had the lowest sum of squared errors, making it the best fit for the data.

In order to determine if the de-correlation lengths and variances used in the ℓGP were reasonable, a semivariogram analysis of the data was performed (Figure 5 b and c). In the semivariogram, a best fit spherical theoretical function⁴⁰ was plotted. From the semivariogram, two sill are visible, one at 500m, and one at 1600m, whereas the nugget semivariance appears to be 0.8, whereas the spatio-temporal variance lies between 2 and 3. From the best fit theoretical function, the parameters were found to be $M_x = M_y = 1537\text{m}$, $\sigma_n^2 = 0.90$, $\sigma_c^2 = 1.37$. Future ℓGP variables can be picked from the semivariogram, either from the fit

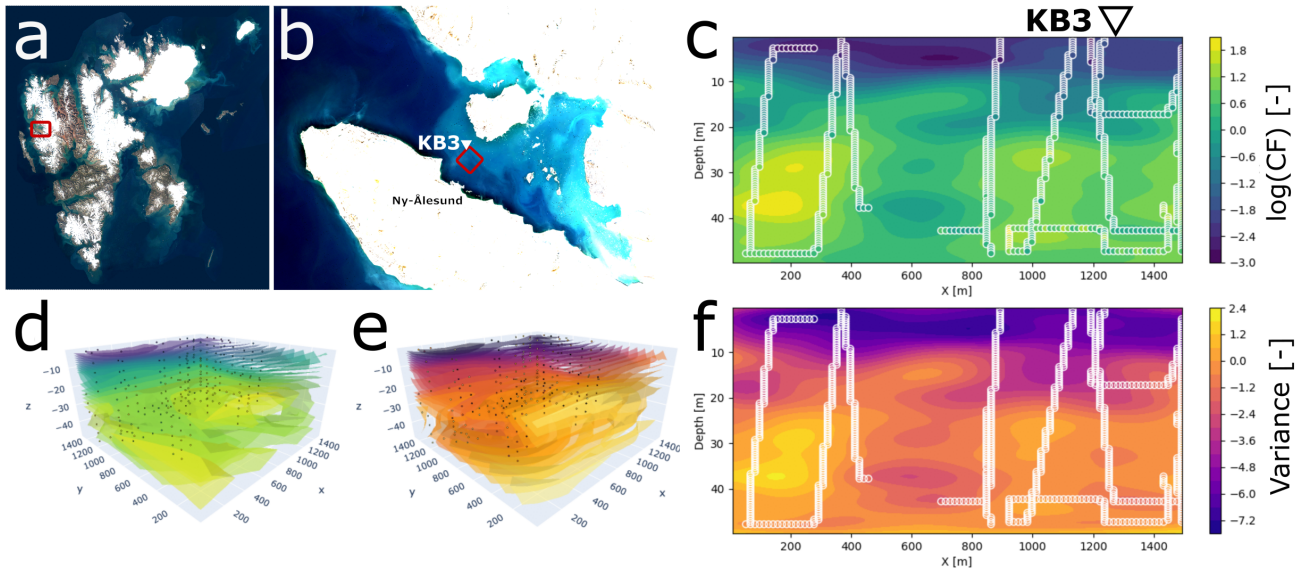


Figure 2. Overview of the operational area of the field trials, and instances of the predicted CF distribution in the operational volume. Satellite overview images of (a) Svalbard (copyright: Norwegian Polar Institute) and (b) Kongsfjorden (from European Space Agency, Sentinel-2 imagery from the 29th of May 2022), with the operational area marked in red, and station KB3 indicated by a white triangle. Predictive mean CF (c,d), and variance (e,f), of the ℓ GP, of the operational volume (c,e) and a horizontal slice (d,f), 300m wide, over the interval $y \in [1200, 1500]$ m. Plotted in log-scale for visualisation, with circles (c-f) indicating grid cells that contain measurements. All field deployment data from AUVs is from 28th of May 2022.

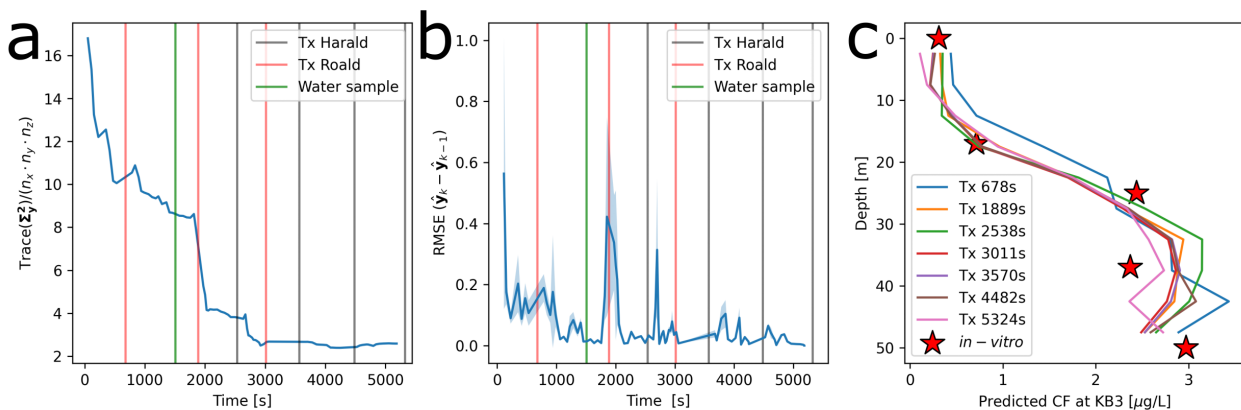


Figure 3. Model performance during field deployment, with water sampling and data exchange sending (Tx) events marked. Averaged (a) prediction uncertainty of each grid cell, (b) prediction error in relation to next prediction for all cells, and synthetic (c) CF profiles at station KB3, after each data exchange event, along with the *in-vitro* chlorophyll a values from water samples. Names (a and b) "Harald" and "Roald" refers to the two AUVs used in the field deployment.

Table 1. Best-fit analysis scores for data set using log-normal, gamma, beta, Burr and normal distributions as candidates.

Distribution	sum of squared errors	Akaike information criterion
log-normal	0.028270	878.292122
gamma	0.031805	926.462837
beta	0.032182	925.454839
Burr	0.037106	867.410520
normal	0.157564	1536.448687

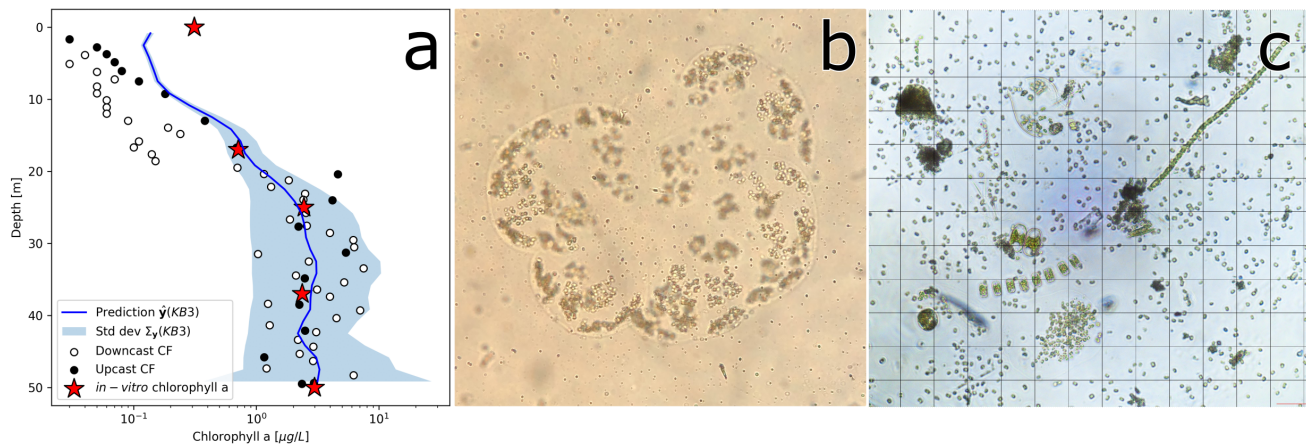


Figure 4. Bloom conditions, (a) a comparison of predicted profile of CF from the ℓ GP and its one standard deviation, ship borne CF measurements on both down- and upcast and *in-vitro* chlorophyll a values from water samples at station KB3 at 11:47 local time on the 28th of May 2022. Colony (b) of *Phaeocystis pouchetii* and an (c) example of the phytoplankton community present in the bloom, both (b and c) microscope images. Photos: (b) Ane Cecilie Kvernvik and (b) Anette Wold.

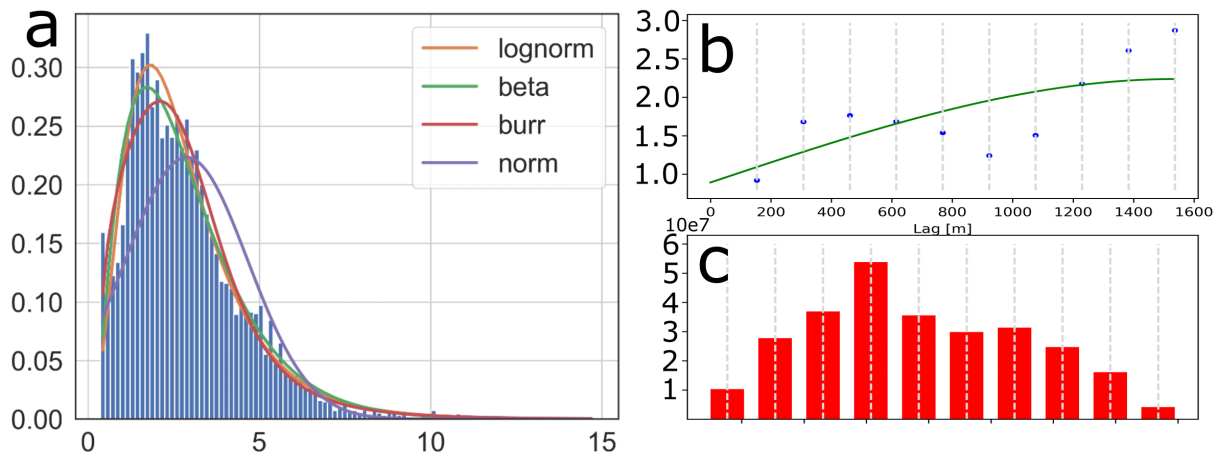


Figure 5. Statistical properties, (a) a histogram of raw CF data along with fitted log-normal, Burr, beta, and normal probability density functions for the entirety of the data set from the 28th of May 2022. Semivariogram (b), with data points plotted in blue dots and the a theoretical best fit function as a green line, and histogram (c) over number of samples for each lag bin, with each bar corresponding to a data point in (b). Semivariogram and histogram were generated using a random sample of 25% of the data.

theoretical function or the data, or an educated combination of the two.

Discussion

We have shown that a 3D adaptive sampling network can provide near real time data updates to operators, both in simulation and in field trials. For the duration of the mission, the underwater vehicles in the network were able to adapt to and monitor the CF field within the operational volume. Acting on the data sent from the AUVs, operators were able to measure and verify the predicted CF profile at the sampling location KB3³⁵, in Kongsfjorden, Svalbard.

The simulation study showed an increase in model accuracy and a decrease in model convergence time when using more than one autonomous vehicle within the same operational area. However, this was done using a static underlying field which could skew the results towards higher accuracy and precision than a dynamic underlying field. Despite of this, the findings hold true, model accuracy increases with the number of vehicles in the same area, with a smaller increase in model accuracy per vehicle for each vehicle added. Further, the simulated CF field contained two large scale patches (Figure 1b), these did not mimic the small scale heterogeneity of the CF measurements observed in the field trials, yet, the large scale patchiness carry similar characteristics. The RMSE, when using a sufficient number of vehicles, converged towards the inherent process and sensor noise, a lower value would be hard to achieve without changing the model parameters. By using a Gaussian method, the model naturally became smoothed and "compressed", not exhibiting the extremes of the measurements in the predictive mean. This effect is also visible in the field trial data (Figure 2c and d).

Comparing the vertical profiles from AUVs, work boat, and *in vitro* measurements (Figure 4a), the measurements and predictions follow each other well below 20m. In the upper 15m, the work boat CF measurements fall out of the error bars of the prediction. The discrepancy between model prediction and work boat CF measurements may have several origins; (1) inaccurate sensor calibration, (2) the model prediction uncertainty, erring on the positive side (equation (6)), and (3) measurements were not co-located and contemporaneous. The small surface discrepancy, $\approx 0.1 \mu\text{g/L}$, between CF measurements and *in vitro* chlorophyll a can be explained by *non-photochemical quenching* (NPQ)⁴¹, a phenomenon in which the amount of measured CF and amount of intracellular chlorophyll a does not match the calibration of the sensor. Since the discrepancy is largest in the surface, where the light is strongest, NPQ is a likely candidate for explanation. There is also a temporal and vertical distance between work boat CF measurements and water sampling, increasing the probability of the discrepancy to originate from spatio-temporal process noise.

From observations gathered during the field campaign, it was indicated that the predominant species of the algal bloom at the time of sampling was *Phaeocystis pouchetii*. Patches or colonies of *P. pouchetii* would be within one sampling envelope of a chlorophyll a fluorometer ($\approx 3 \text{ ml}$ ⁴²), but would be integrated in the 10L Niskin bottle sample. This helps to explain the relative difference in noise level of the *in situ* CF measurements and the *in vitro* samples of chlorophyll a (Figure 4a). The values from *in vitro* samples also fits the predicted values from the *in situ* CF gathered by the AUVs, where the uncertainty reflects the noise in the data. In addition, the *in vitro* samples were pseudoreplicated, with a variance of $\approx 0.01 [\mu\text{g}^2/\text{L}^2]$, within each sample. This is negligible in relation to the variance of the *in situ* CF measurements. The noise could also be caused by the low signal-to-noise ratio from fluorescence sensors, irradiance from the sun, different species of algae, photosynthetic rate, and health of the cells⁴³.

The assumption of a log-normal CF distribution^{2,29} was verified (Figure 5), however, the input to the ℓ -GP is the cell-averaged CF values, not the raw measurements. When attempting a best-fit analysis on the segmented data, the results were less clear, with no obvious best fit distribution. A criticism to the best-fit analysis, is that the data is collected adaptively, seeking to maximize the CF value, and reduction in uncertainty (dependent on the CF value), thereby skewing the data in favour of higher values, thus skewing the histogram.

From the fit theoretical function in the variogram (Figure 5b), the nugget and variance was found to be within reasonable range from the initial heuristic values. The nugget effect used was smaller than the one presented in the data, while the variance used was higher than the one used in the model. The horizontal de-correlation length predicted from the variogram, 1537m, is substantially longer than the de-correlation length used in the on board model, 600m. However, from the variogram data, there seems to be two predominant de-correlation lengths, the longer at 1537m and a shorter at around 500m. In choosing a shorter horizontal length scale, the model might over-estimate the uncertainty, but is more apt at preserving heterogeneity in the data. In the semivariogram, time was not taken into account, as the total mission time was less than two hours, and thus we can assume it to be fairly static^{3,4,28}.

Conclusion and further work

Our data shows that real-time data reported by multiple collaborating autonomous underwater vehicles combined with targeted water sampling can significantly increase our understanding of plankton patchiness. A method for adaptive tracking of CF based on a log-Gaussian process as a lightweight ocean model for a sensing network of AUVs and a boat was presented. The

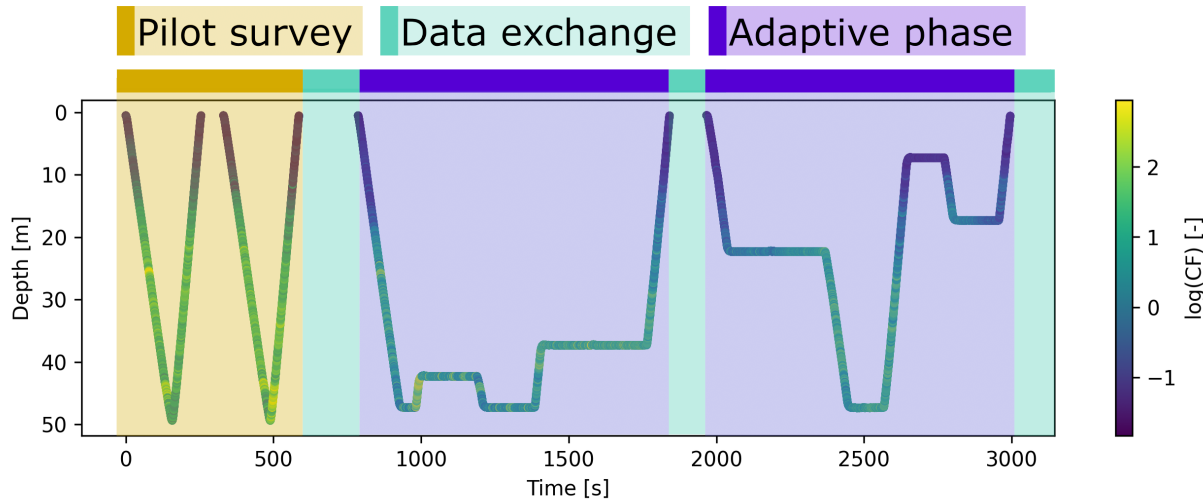


Figure 6. Timeline of LAUV Roald on the 28th of May 2022, depth plotted against time, with color indicating the value of CF, plotted as $\log(\text{CF})$ for visualization.

method models the chlorophyll a abundance, inferred by *in-situ* fluorescence measurements made by the underwater vehicles. The AUVs were able to detect, explore, and measure the CF field inside the *operational volume* for the duration of the mission. The information relayed to the boat was acted upon and water samples and *in-situ* CF measurements were taken from the boat. By enabling on-board adaption, coupled with a small-bandwidth satellite communication, the vehicles were able to make decisions *in-situ*, targeting the desired combination of uncertainty reduction and CF maxima-seeking. By adding temporally increasing noise to the measurements, the on-board ℓGP model was able to increase the significance of the most recent measurements. In doing multi vehicle adaptive sampling with data sharing, the vehicles are forced to communicate, with the added benefit of allowing the operator to observe the data and communications in real time. Having an active operator, acting upon the information received, it was showed that targeted sampling of the water-column were enriched by the field estimates. In future work, including covariates, such as CTD, currents, radiance, and remote sensing should be considered, providing a more holistic picture of the region of interest. Longer duration deployments in varying bloom conditions should be undertaken to further robustify the method by collecting data on spatial and temporal length-scales in a diverse set of scenarios, leading to a more well-calibrated model and utility function. Further work should also include a more formal configuration of the path-finding parameters in Equation (8), optimizing for the desired behavior in a multitude of bloom scenarios.

More information on pelagic biodiversity is urgently needed as the demand on these resources increases from climate change and harvesting. Future integration with automated eDNA samplers, such as LRAUV-ESP⁴⁴, or imaging instruments⁴⁵, together with adaptive sampling technologies reporting in real-time can be used to contextualize and inform plankton community sampling. Filling important knowledge gaps and observe complex biological processes at fine-scale temporal and spatial resolutions.

Methods and materials

The method was centered around the *on-board algorithm* used for adaptive behavior and data exchange, developed using simulation and field tested. The *on-board algorithm* consists of (a) the pre-defined *pilot survey*, (b) the *data exchange*, and (c) the *adaptive phase*. The *adaptive phase* was further subdivided in (i) the on-board model and (ii) the path planning. For the AUVs, the mission was initialized by executing a pilot survey, followed by a data exchange. After this initial phase, the adaptive phase ran for a fixed period before a data exchange was performed and the adaptive phase started again (Figure 6). The *sampling network* used the data gathered by the AUVs for informed sampling from a manned craft. Adaptive path planning was done on-board the autonomous vehicles, providing robustness to communication loss and enabling *in-situ* decision making.

On-board algorithm: Pilot survey

A rectangular cuboid was selected as the *operational volume* shape for exploration, and the *operational area* is the projection on the horizontal plane of this volume. The size and orientation of the volume is commonly decided by the operator, depending on the nature of the mission, number of available vehicles, their speed, and the desired spatiotemporal model accuracy³². The *pilot survey*⁴, is usually a pre-planned path, designed to gather data for the initialization of the on-board model. In this case, we set it

Table 2. Overall message structure with the header in the first 10 bytes and the data in the remaining, depending on available data and SBD limitations. Data message structure for $n_c = 1$, cell number is sent as a UInt16, as the number of grid cells should be in the interval 256 to 65536, and where $k \in [0, \dots, l_d)$ is the data index.

Field	message ID	vehicle ID	lat	lon	data	Cell no.	Time
Start byte	0	1	2	6	$10 + kn_d$	$11 + kn_d$	$13 + kn_d$
Data type	UInt8	UInt8	Float32	Float32	UInt8	UInt16	UInt8

as a crossing of the operational area by all the AUVs in the system, where the path is determined by the number of vehicles, N_v , in the network. All vehicles were set to cross from $y = 0$ to y_{max} in parallel paths. The x -value of the path was determined by

$$x_v = V_x \frac{2 \cdot n_v + 1}{2 \cdot N_v} \quad (1)$$

for vehicle n_v of N_v , where n_v is 0-indexed, and V_x was the x-extent of the operational area. The *pilot survey* path undulated between the surface and the maximal depth of the operational volume. After the *pilot survey*, the data collected was segmented and sent to the *operator hub* in a surfacing event, where the vehicle received data available from other vehicles in a *data exchange* phase.

On-board algorithm: Data exchange

As data is collected at high rates on different platforms, it was segmented in order to fit the pre-defined message structure; enabling computational feasibility of the on-board model and low-bandwidth data sharing. The segmentation used the shared knowledge of the agents about the operational area, whereas the *data exchange* used the segmented data for efficient low-bandwidth communication.

Segmentation

For computational feasibility of the on-board model, the number of samples usually needs to be restrained to below $\sim 10000^{27}$. The measurements were segmented into a $n_x \times n_y \times n_z$ grid, reducing the maximum sample size to $n_x \cdot n_y \cdot n_z$ and creating a 3D grid in the operational volume. The number of grid cells was decided by the operator, and could be adjusted according to desired resolution and the available on-board computing power. All the agents shared one commonly defined grid. For each iteration in the adaptive phase, the measurements collected were assigned to their respective grid cell. The data value of that cell was set to the average of the measurements taken within that cell since the last segmentation. Previous measurements were discarded if new data was collected within that cell. We assumed that temporal de-correlation would make previous measurements irrelevant compared to the new measurements. Cells with previous held data values and no new measurements kept their data intact. Data segmentation was performed at each update step, before evaluation of the on-board model and adaption.

Exchange

The AUVs surfaced at regular intervals, transmitting the latest segmented data, following the flowchart in Figure 7a. The surfacing event served two main purposes, (1) to exchange data with the other vehicles in the system, and (2) to get a GPS fix to bound the navigational uncertainty of the vehicle. The data, vehicle position, and time were transmitted via IRIDIUM®^{30,31} short-burst data (SBD) to a central *operator hub*, where the operator monitored the operation and data flow. The *operator hub* then responded to the vehicle with the most recent data and positions received from the other agents in the system. The IRIDIUM® SBD protocol limits the message size to 340 bytes^{30,31}, while the vehicle specific driver needed 20 bytes for overhead. Data for one grid cell took up $n_d = 3 + n_c$ bytes, where n_c is the number of data channels (e.g. fluorescence, dissolved oxygen, temperature, salinity), creating the message structure (Table 2). This enabled the sending of up to $l_d = \lfloor \frac{320}{n_d} \rfloor$ data points over IRIDIUM® SBD.

If the queue of unsent data points was longer than l_d , the message was truncated to contain the l_d newest data points. The *operator hub* also dispatched a message containing the last known positions of the other vehicles in the network to the surfaced vehicle. This message was not as constrained in size as the data message, given that the number of vehicles, N_v , is sufficiently small.

Operator Hub

As the communication center in the sampling network, the *operator hub* distributed the information throughout the sampling network, both to AUVs and operators. Data was transmitted to the *operator hub* and presented to the operators both as raw

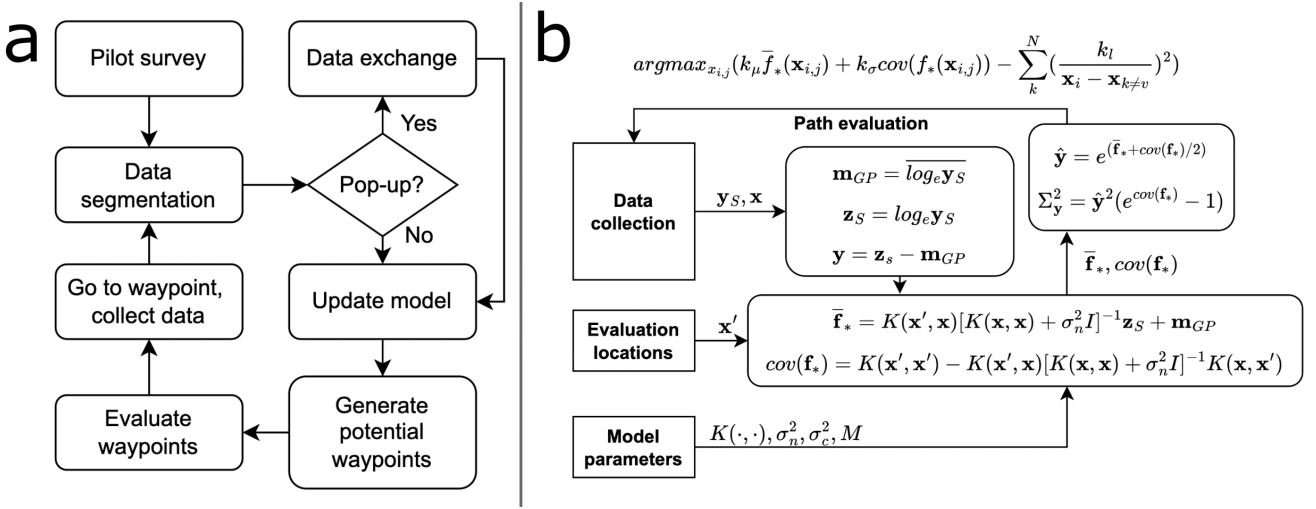


Figure 7. Overview of the *on-board algorithm*. Flowcharts of the (a) *on-board algorithm*, starting at the *pilot survey*, followed by the cyclical *data exchange* and *adaptive phases*, and (b) *adaptive phase*, with data ingestion, ℓ GP evaluation at potential waypoints, \mathbf{x}' , and their evaluation.

messages, and the ℓ GP realization, with the latest vehicle position. From there, the operator could interrogate the model for a predicted profile anywhere in the operational area along with its error bounds. Based on this, the operators could choose to act on the information and perform targeted sampling, having a greater understanding of the contextual data field. The act of sending the data near real time through the operator hub enabled a 'human-in-the-loop' approach. When the data exchange was completed, the vehicles updated the model and began the adaptive phase.

On-board algorithm: Adaptive phase

In the adaptive phase, the available data was used as training data for a GP²⁷, in the form of a ℓ GP^{2,4}. Potential paths were generated from a set of potential waypoints around the vehicle and deliberated upon using the predictive mean and variance at the waypoint. In addition, its proximity to other vehicles in the area was taken into account. When the vehicle reached the desired waypoint, a new waypoint was chosen by the same means until it was time for a *data exchange*.

On-board model

The ℓ GP^{2,4,27} was expanded to three physical dimensions and time-varying uncertainty was added to the measurements. We denoted set of measurements \mathbf{y}_S at locations X at times τ , with $S = [X, \tau]$ and let $\mathbf{z}_S = \log_e \mathbf{y}_S - \mathbf{m}_{GP}$, where $\mathbf{m}_{GP} = \bar{\log_e y}_S$ was the mean of the input data. In taking the logarithm of the measurements, they became unit-less⁴⁶. We assumed that $\mathbf{z}_S \sim \mathcal{N}(\mu, \sigma_c^2)$, such that a GP could be used for predictions of \mathbf{z} at unobserved locations and times by the formulation in equations (2) to (4)²⁷.

$$\mathbf{f}_*|S, \mathbf{z}_S, S_* \sim \mathcal{N}(\bar{\mathbf{f}}_*, cov(\mathbf{f}_*)), \text{ where} \quad (2)$$

$$\bar{\mathbf{f}}_* \triangleq \mathbb{E}[\mathbf{f}_*|S, \mathbf{z}_S, S_*] = K_{S, S_*}[K_{S, S} + \sigma_n^2 I]^{-1} \mathbf{z}_S + \mathbf{m}_{GP} \quad (3)$$

$$cov(\mathbf{f}_*) = K_{S, S_*} - K_{S, S_*}[K_{S, S} + \sigma_n^2 I]^{-1} K_{S, S_*} \quad (4)$$

Where $S_* = [X_*, \tau_{now}]$ was a set of prediction locations at the time of the prediction, τ_{now} , $\bar{\mathbf{f}}_*$ was the predictive mean at locations S_* , and $K_{u,v}$ was the kernel function evaluated at locations u and v , and σ_n^2 was the nugget variance⁴⁷. The kernel function (equation (5)), where $M = diag([M_x, M_y, M_z, M_\tau])$ is the diagonal matrix of de-correlation lengths for each dimension of \mathbf{s} , including time τ , where \mathbf{s} is a row of S ; one location.

$$k(\mathbf{s}, \mathbf{s}') = \sigma_c^2 e^{-\frac{1}{2} \left| \frac{\mathbf{s} - \mathbf{s}'}{M} \right|^2} \quad (5)$$

Time was included in the kernel function to account for the temporal decay of accuracy in the measurements. This lead to the covariance matrix having to be updated at each evaluation step, further leading to a full evaluation of the GP at each

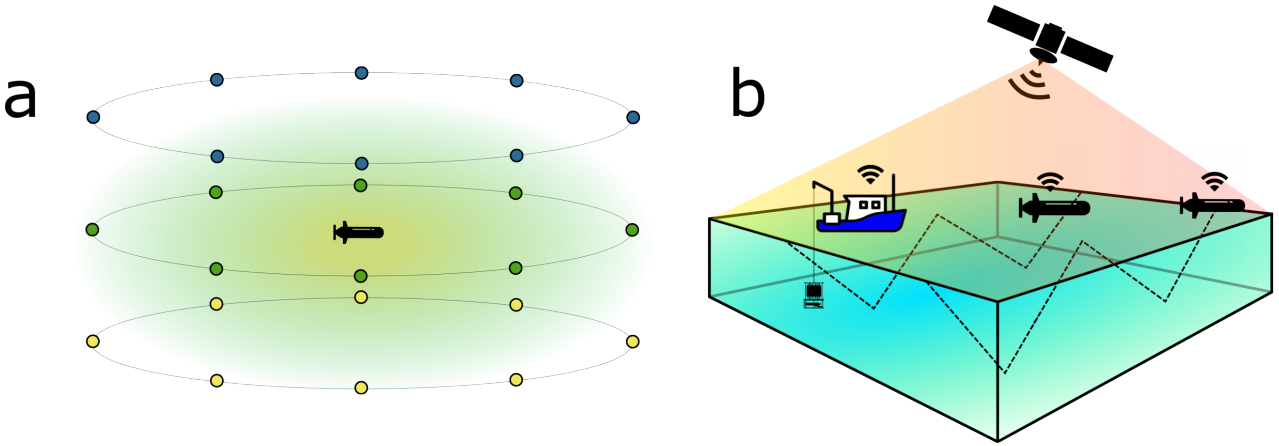


Figure 8. Conceptual illustrations of (a) the potential waypoints generated at every update step by having $n_\theta = 8$ segments, 3 waypoints in the vertical per segment, resulting in 24 potential waypoints around the AUV, and (b) mission setup for the field trials, using two AUVs and a work boat, communicating over satellite.

iteration, in stead of step-wise ingestion of data^{3,26}. In order to produce a predictive mean for the value of CF, the predictive mean for \mathbf{z}_S must be transformed² as presented in equations (6) and (7).

$$\hat{\mathbf{y}} = e^{(\bar{\mathbf{f}}_* + cov(\mathbf{f}_*)/2)} \quad (6)$$

$$\Sigma_y^2 = \hat{\mathbf{y}}^2 (e^{cov(\mathbf{f}_*)} - 1) \quad (7)$$

From equations (6) and (7) we see that the variance, Σ_y^2 , is dependent on the predictive mean, unlike for the linear GP. This needs to be taken into account when evaluating the potential paths for optimal, adaptive sampling.

Path planning

After data was ingested into the ℓ GP, it was evaluated at potential waypoint locations, in order to find the optimal path. Using the current position of the AUV, \mathbf{x}_v , as the center, it created $3n_\theta$ potential waypoint locations, where n_θ is the number of segments uniformly spread around a circle. These locations were generated as $\mathbf{x}_{i,j} = \mathbf{x}_v + [r\cos\theta_i, r\sin\theta_i, \Delta z_j]$, where $\Delta z = [-z_d, 0, z_d]$, \mathbf{x}_v is the vehicle position at the current time, r is a radius, and z_d is the vertical extent of one grid cell (Figure 8a). Each of the potential locations were screened to see if they were inside the operational volume, and the ones who fell outside were discarded. Then, the predictive mean and uncertainty at the potential locations were evaluated along with the distance from the location, $\mathbf{x}_{i,j}$, to the last known location of the other vehicles. The optimal waypoint maximized equation (8).

$$argmax_{x_{i,j}} (k_\mu \hat{\mathbf{y}}(\mathbf{x}_{i,j}) + k_\sigma \Sigma_y^2(\mathbf{x}_{i,j}) - \sum_k^N (\frac{k_l}{\mathbf{x}_i - \mathbf{x}_{k \neq v}})^2) \quad (8)$$

The constants k_μ , k_σ , and k_l were configuration parameters, enabling the operator to choose the weight of each element of the evaluation function. Tuning of k_μ and k_σ was done in simulation, where the trade-off between uncertainty reduction and maxima-seeking could be set by the operators. Setting k_l is a function of how close the operator wants the vehicles to come to each other, and in deciding its value, the speed of the vehicles and the size of the operational area needs to be taken into account³². Notice that only the horizontal distance between the vehicles was taken into account, as the vertical extent of the operational volume usually is far less than the horizontal. After the optimal waypoint was chosen, the AUV travelled towards it, collecting underway measurements. Then, when the waypoint was reached, the measurements were segmented, the ℓ GP evaluated, and a new waypoint chosen.

Simulation and field deployment

The method was developed and tested using a simulated CF field along with the vehicle simulator in DUNE (DUNE: Unified Navigation Environment)⁴⁸. Constellations of multiple AUVs were simulated using a virtual machine for each vehicle, using

Table 3. Operator inputs, with values used for field trials and their explanation.

Variable	Value	Explanation
$[V_x, V_y, V_z]$	[1500, 1500, 50]m	Operational volume extent in [x,y,z]-directions.
$[V_{lat}, V_{lon}, V_\theta]$	[78N 57.29, 11E 56.85, -45°]	[Latitude, longitude, orientation] of operational volume origin.
$[n_x, n_y, n_z]$	[15, 15, 10]	Operational volume number of grid points in [x,y,z]-directions.
$[M_x, M_y, M_z]$	[600, 600, 3]m	De-correlation length in [x,y,z]-directions.
M_τ	10000s	De-correlation time.
$[\sigma_c, \sigma_n]$	[1.6, 0.7]	[Variance,nugget] uncertainties of \mathbf{z}_S , from previous data ³ .
$[k_\mu, k_\sigma, k_l]$	[1, 1, 300m]	Configuration parameters of path evaluation function.

the host computer as the operator hub, and emulating satellite communication by reading and writing to a shared directory on the host computer. A field deployment was carried out during the Arctic spring bloom, on the 28th of May of 2022 in Kongsfjorden, Svalbard, focusing on an area around sampling station KB3³⁵. Operator input values (Table 3) for the above presented method were chosen based on simulation trials and prior assumptions^{29,49}. Values are common to simulation and field deployment, except the operational volume x - and y -extent. A conceptual overview of the operational setup is presented in Figure 8b.

Vehicles and Sensors

The *on-board algorithm* was implemented on two Light AUVs (LAUVs)⁴⁸, using their backseat driver⁵⁰. The LAUV concept was developed at the Underwater Systems and Technology Laboratory at the University of Porto, and commercially produced by OceanScan Marine Systems and Technology Lda. The vehicles, LAUVs "Harald" and "Roald" (AUR-Lab, NTNU), and are equipped with a scientific payload of a CTD sensor, and a chlorophyll a fluorometer. Specifically, LAUV "Roald" is equipped with a RBR Turner Cyclops Fluorometer and an AML Smart X CTD, while LAUV "Harald" carries a WetLabs EcoPuck Triplet and a SBE 49 FastCAT CTD. The on-board software, DUNE, (also used for simulation) controls the navigation, sensors, and low-level control and guidance on the vehicle. A manned work boat, R/V Teisten (Kings Bay AS), was used as the platform for targeted sampling. It was equipped with a SAIV SD204 CTD with a Seapoint chlorophyll a *in situ* Fluorometer, 300m-capable winch and 10L Niskin bottle water samplers⁵¹.

In vitro sampling

A subsurface CF maximum could be biased by NPQ, exhibiting as a subsurface peak, by quenching the signal close to the surface rather than representing the true distribution of chlorophyll a in the water column. We compared CF predictions from *in situ* AUV data and shipborne CF measurements with the *in vitro* concentrations of chlorophyll. To validate the data retrieved from sensors, discrete water samples for measurement of *in vitro* chlorophyll a were collected using 10 L Niskin bottles⁵¹ on board the work boat. Sample depths were selected based on layers of high, medium and low CF as estimated by the model generated in the operator hub from data from the AUVs. Seawater was filtered (0.5 L) onto Whatman GF/F glass fiber filters¹⁷. In the laboratory, chlorophyll a was extracted in 100% methanol after 20 hours at -20°C in darkness. The chlorophyll a concentrations were determined using a Turner Designs Trilogy fluorometer (model: 7200-000) following the non-acidification method⁵².

Data availability

The data generated and analysed during the current study is available from the corresponding author.

References

1. McQuatters-Gollop, A. *et al.* Is there a decline in marine phytoplankton? *Nature* **472**, E6–E7 (2011).
2. Low, K. H., Dolan, J., Schneider, J. & Elfes, A. Multi-robot adaptive exploration and mapping for environmental sensing applications. *PhD thesis, CMU* (2009).
3. Fossum, T. O. *et al.* Toward adaptive robotic sampling of phytoplankton in the coastal ocean. *Sci. Robotics* **4** (2019).
4. Kemna, S. *Multi-robot strategies for adaptive sampling with autonomous underwater vehicles*. Ph.D. thesis, thesis, University of Southern California (2018).
5. Falkowski, P. G. The role of phytoplankton photosynthesis in global biogeochemical cycles. *Photosynth. research* **39**, 235–258 (1994).

6. Trudnowska, E. *et al.* Marine snow morphology illuminates the evolution of phytoplankton blooms and determines their subsequent vertical export. *Nat. communications* **12**, 1–13 (2021).
7. Sakshaug, E., Johnsen, G. H. & Kovacs, K. M. *Ecosystem Barents Sea* (Tapir Academic Press, 2009).
8. Falkowski, P. G. & Raven, J. A. *Aquatic photosynthesis* (Princeton University Press, 2013).
9. Grünbaum, D. The logic of ecological patchiness. *Interface Focus*. **2**, 150–155 (2012).
10. Robinson, K. L., Sponaugle, S., Luo, J. Y., Gleiber, M. R. & Cowen, R. K. Big or small, patchy all: Resolution of marine plankton patch structure at micro-to submesoscales for 36 taxa. *Sci. advances* **7**, eabk2904 (2021).
11. Mitchell, J. G., Yamazaki, H., Seuront, L., Wolk, F. & Li, H. Phytoplankton patch patterns: seascape anatomy in a turbulent ocean. *J. Mar. Syst.* **69**, 247–253 (2008).
12. Durham, W. M. & Stocker, R. Thin phytoplankton layers: characteristics, mechanisms, and consequences. *Annu. review marine science* **4**, 177–207 (2012).
13. Van Gennip, S. *et al.* Plankton patchiness investigated using simultaneous nitrate and chlorophyll observations. *J. Geophys. Res. Ocean.* **121**, 4149–4156 (2016).
14. Schalles, J. F. Optical remote sensing techniques to estimate phytoplankton chlorophyll a concentrations in coastal. In *Remote sensing of aquatic coastal ecosystem processes*, 27–79 (Springer, 2006).
15. Dierssen, H. M. Perspectives on empirical approaches for ocean color remote sensing of chlorophyll in a changing climate. *Proc. Natl. Acad. Sci.* **107**, 17073–17078 (2010).
16. Wassmann, P., Ratkova, T. & Reigstad, M. The contribution of single and colonial cells of *phaeocystis pouchetii* to spring and summer blooms in the north-eastern north atlantic. *Harmful algae* **4**, 823–840 (2005).
17. Fragoso, G. M. *et al.* Contrasting phytoplankton-zooplankton distributions observed through autonomous platforms, in-situ optical sensors and discrete sampling. *Plos one* **17**, e0273874 (2022).
18. McGann, C. *et al.* T-rex: A model-based architecture for auv control. In *3rd Workshop on Planning and Plan Execution for Real-World Systems*, vol. 2007 (2007).
19. Zhang, Y., Ryan, J. P., Bellingham, J. G., Harvey, J. B. & McEwen, R. S. Autonomous detection and sampling of water types and fronts in a coastal upwelling system by an autonomous underwater vehicle. *Limnol. Oceanogr. Methods* **10**, 934–951 (2012).
20. Zhang, Y., Bellingham, J. G., Ryan, J. P., Kieft, B. & Stanway, M. J. Two-dimensional mapping and tracking of a coastal upwelling front by an autonomous underwater vehicle. In *2013 OCEANS-San Diego*, 1–4 (IEEE, 2013).
21. Zhang, Y., Bellingham, J. G., Ryan, J. P., Kieft, B. & Stanway, M. J. Autonomous four-dimensional mapping and tracking of a coastal upwelling front by an autonomous underwater vehicle. *J. Field Robotics* **33**, 67–81 (2016).
22. Zhang, Y. *et al.* Autonomous tracking and sampling of the deep chlorophyll maximum layer in an open-ocean eddy by a long-range autonomous underwater vehicle. *IEEE J. Ocean. Eng.* (2019).
23. Fossum, T. O. *Adaptive Sampling for Marine Robotics*. Ph.D. thesis, Norwegian University of Science and Technology (2019).
24. Fossum, T. O. *et al.* Adaptive sampling of surface fronts in the arctic using an autonomous underwater vehicle. *IEEE J. Ocean. Eng.* (2021).
25. Fossum, T. O., Travellietti, C., Eidsvik, J., Ginsbourger, D. & Rajan, K. Learning excursion sets of vector-valued gaussian random fields for autonomous ocean sampling. *The Annals Appl. Stat.* **15**, 597–618 (2021).
26. Stankiewicz, P., Tan, Y. T. & Kobilarov, M. Adaptive sampling with an autonomous underwater vehicle in static marine environments. *J. Field Robotics* **38**, 572–597 (2021).
27. Rasmussen, C. E. Gaussian processes in machine learning. In *Summer School on Machine Learning*, 63–71 (Springer, 2003).
28. Berget, G. E., Fossum, T. O., Johansen, T. A., Eidsvik, J. & Rajan, K. Adaptive sampling of ocean processes using an auv with a gaussian proxy model. *IFAC-PapersOnLine* **51**, 238–243 (2018).
29. Kemna, S., Caron, D. A. & Sukhatme, G. S. Adaptive informative sampling with autonomous underwater vehicles: Acoustic versus surface communications. In *OCEANS 2016 MTS/IEEE Monterey*, 1–8 (IEEE, 2016).
30. Maine, K., Devieux, C. & Swan, P. Overview of iridium satellite network. In *Proceedings of WESCON'95*, 483 (IEEE, 1995).

31. Pratt, S. R., Raines, R. A., Fossa, C. E. & Temple, M. A. An operational and performance overview of the iridium low earth orbit satellite system. *IEEE Commun. Surv.* **2**, 2–10 (1999).
32. Leonard, N. E. *et al.* Collective motion, sensor networks, and ocean sampling. *Proc. IEEE* **95**, 48–74 (2007).
33. Bhatta, P. *et al.* Coordination of an underwater glider fleet for adaptive ocean sampling. In *Proc. International Workshop on Underwater Robotics, Int. Advanced Robotics Programmed (IARP)*, Genoa, Italy (Citeseer, 2005).
34. Gat, E., Bonnasso, R. P., Murphy, R. *et al.* On three-layer architectures. *Artif. intelligence mobile robots* **195**, 210 (1998).
35. Renaud, P. E., Tessmann, M., Evensen, A. & Christensen, G. N. Benthic food-web structure of an arctic fjord (kongsfjorden, svalbard). *Mar. Biol. Res.* **7**, 13–26 (2011).
36. Hop, H. & Wiencke, C. The ecosystem of kongsfjorden, svalbard. In *The Ecosystem of Kongsfjorden, Svalbard*, 1–20 (Springer, 2019).
37. Cokelaer, T. Python fitter package (2022).
38. Burr, I. W. Cumulative frequency functions. *The Annals mathematical statistics* **13**, 215–232 (1942).
39. Stoica, P. & Selen, Y. Model-order selection: a review of information criterion rules. *IEEE Signal Process. Mag.* **21**, 36–47 (2004).
40. Mälicke, M., Möller, E., Schneider, H. D. & Müller, S. mmaelicke/scikit-gstat: A scipy flavoured geostatistical variogram analysis toolbox, DOI: <http://doi.org/10.5281/zenodo.4835779> (2021).
41. Muller, P., Li, X.-P. & Niyogi, K. K. Non-photochemical quenching. a response to excess light energy. *Plant physiology* **125**, 1558–1566 (2001).
42. Boss, E. & Haëntjens, N. Primer regarding measurements of chlorophyll fluorescence and the backscattering coefficient with wetlabs flbb on profiling floats. (2016).
43. Johnsen, G., Bricaud, A., Nelson, N., Prézelin, B. & Bidigare, R. In vivo bio-optical properties of phytoplankton pigments. *Phytoplankton pigments: Charact. chemotaxonomy applications oceanography* 497–537 (2011).
44. Yamahara, K. M. *et al.* In situ autonomous acquisition and preservation of marine environmental dna using an autonomous underwater vehicle. *Front. Mar. Sci.* **6**, 373 (2019).
45. Davies, E. J., Brandvik, P. J., Leirvik, F. & Nepstad, R. The use of wide-band transmittance imaging to size and classify suspended particulate matter in seawater. *Mar. pollution bulletin* **115**, 105–114 (2017).
46. Matta, C. F., Massa, L., Gubskaya, A. V. & Knoll, E. Can one take the logarithm or the sine of a dimensioned quantity or a unit? dimensional analysis involving transcendental functions. *J. Chem. Educ.* **88**, 67–70 (2011).
47. Cressie, N. & Wikle, C. K. *Statistics for spatio-temporal data* (John Wiley & Sons, 2015).
48. Sousa, A. *et al.* Lauv: The man-portable autonomous underwater vehicle. *IFAC Proc. Vol.* **45**, 268–274 (2012).
49. Fossum, T. O. *et al.* Information-driven robotic sampling in the coastal ocean. *J. Field Robotics* **35**, 1101–1121 (2018).
50. Pinto, J., Mendes, R., da Silva, J. C., Dias, J. M. & de Sousa, J. B. Multiple autonomous vehicles applied to plume detection and tracking. In *2018 OCEANS-MTS/IEEE Kobe Techno-Oceans (OTO)*, 1–6 (IEEE, 2018).
51. Niskin, S. J. (Jan. 13, 1970).
52. Holm-Hansen, O. & Riemann, B. Chlorophyll a determination: improvements in methodology. *Oikos* 438–447 (1978).

Acknowledgements

The research presented in this paper was funded by the Research Council of Norway through the Nansen Legacy project RCN #276730, the Center of Excellence Autonomous Marine Operations and Systems (AMOS), RCN #223254, and Light as a Cue for Life in Arctic and Northern Seas (LightLife), RCN #315728. Thank you to Kings Bay AS for providing helpful service and instrumentation.

Author contributions statement

T.M.B. conceived the experiment, with help from S.M. and G.M.F. T.M.B., M.L., and S.M. conducted the experiment, and T.M.B. and S.M. analysed the results. T.M.B. wrote the manuscript with input from S.M. and G.M.F. on introduction and S.M. on results, discussion, and conclusion. All authors reviewed the manuscript.

Additional information

Correspondence and requests for materials should be addressed to T.M.B.

Competing interests: the authors declare no competing interests.

The corresponding author is responsible for submitting a [competing interests statement](#) on behalf of all authors of the paper. This statement must be included in the submitted article file.